

# Scalable non-volatile tuning of photonic computational memories by automated silicon ion implantation

*Akhil Varri, Shabnam Taheriniya, Frank Brückerhoff-Plückelmann, Ivonne Bente, Nikolaos Farmakidis, Daniel Bernhardt, Harald Rösner, Maximilian Kruth, Achim Nadzeyka, Torsten Richter, Christopher David Wright, Harish Bhaskaran, Gerhard Wilde\*, and Wolfram H.P. Pernice\**

A. Varri, F. Brückerhoff-Plückelmann, I. Bente, W.H.P. Pernice  
Institute of Physics,  
University of Münster, Heisenbergstr. 11, 48149 Münster, Germany  
Email: wolfram.pernice@kip.uni-heidelberg.de

A. Varri, F. Brückerhoff-Plückelmann, I. Bente, W.H.P. Pernice  
Center for Soft Nanoscience,  
University of Münster, Busso-Peus-Street 10, 48149 Münster, Germany

S. Taherinia, H. Rösner, G. Wilde  
Institute of Materials Physics,  
University of Münster, Wilhelm-Klemm-Street 10, 48149 Münster, Germany  
Email: gwilde@uni-muenster.de

S. Taherinia, W.H.P. Pernice  
Kirchhoff-Institute for Physics, Im Neuenheimer Feld 227, 69120 Heidelberg, Germany

N. Farmakidis, H. Bhaskaran  
Department of Materials, University of Oxford, Parks Road, Oxford, UK

D. Bernhardt, A. Nadzeyka, T. Richter  
RAITH Nanofabrication, Konrad-Adenauer-Allee 8, 44263 Dortmund, Germany

M. Kruth  
Ernst Ruska-Centre for Microscopy and Spectroscopy with Electrons and Peter Grünberg  
Institute, Forschungszentrum Jülich, 52425 Jülich, Germany

C.D. Wright  
Department of Engineering, University of Exeter, Exeter EX4 4QF, UK

Keywords: photonic integrated circuits, wavelength division multiplexing, micro-ring resonators, focused ion implantation, electron energy-loss spectroscopy

This article has been accepted for publication and undergone full peer review but has not been through the copyediting, typesetting, pagination and proofreading process, which may lead to differences between this version and the [Version of Record](#). Please cite this article as [doi: 10.1002/adma.202310596](https://doi.org/10.1002/adma.202310596).

This article is protected by copyright. All rights reserved.

## Abstract

Photonic Integrated Circuits (PICs) are revolutionizing the realm of information technology, promising unprecedented speeds and efficiency in data processing and optical communication. However, the nanoscale precision required to fabricate these circuits at scale presents significant challenges, due to the need to maintain consistency across wavelength-selective components, which necessitates individualized adjustments after fabrication. Harnessing spectral alignment by automated silicon ion implantation, in this work scalable and non-volatile photonic computational memories are demonstrated in high quality resonant devices. Precise spectral trimming of large-scale photonic ensembles from few picometers to several nanometres is achieved with long-term stability and marginal loss penalty. Based on this approach spectrally aligned photonic memory and computing systems for general matrix multiplication are demonstrated, enabling wavelength multiplexed integrated architectures at large scales.

## 1. Introduction

The demands for drastically increasing computing power<sup>[1]</sup> combined with the imminent end of transistor scaling<sup>[2]</sup> have been the main drivers for research into alternate computing paradigms. Integrated photonics as a promising platform for neuromorphic computing<sup>[3]</sup>, mixed-precision accelerators<sup>[4,5]</sup>, and quantum computing<sup>[6]</sup>, has garnered heavy attention recently in academia as well as industry<sup>[7–10]</sup>. The rationale of using light for computation

This article is protected by copyright. All rights reserved.

results from advantages in bandwidth, latency, and power consumption. These factors have successfully led to fiber optics revolutionizing the telecommunications industry. Miniaturized photonic circuits which translate manufacturing advances from the Complementary Metal-Oxide-Semiconductor (CMOS) industry to optics have served as a game-changer for implementing optical computing paradigms in a chip-scale setting<sup>[11,12]</sup>. Similarly, rapid developments in silicon photonics have found applications for networking in data centers<sup>[13,14]</sup> with the goal to replace the electrical interconnects in the servers even at shorter distances to meet the ever-increasing demands of big data.

In addition, PICs have also attracted a lot of attention recently<sup>[15–17]</sup> due to their ability to integrate with functional materials such as a phase-change material (PCM). PCMs can be used to alter the phase or amplitude of light via evanescent coupling. These properties can be switched either optically or electrically on a sub-nanosecond timescale and are non-volatile in nature. Hence, their integration with PICs holds significant promise in the push towards optical memories and in-memory computing.

Nevertheless, a key challenge in upscaling integrated photonic systems is the sensitive nature of the components to fabrication imperfections. Since photonic circuits are usually designed to operate in the analogue domain, standard process variations in etching rate, exposure parameters, and chemical mechanical polishing conditions adversely affect their functionality<sup>[18–21]</sup>. For example, a 2% error in the splitting ratio of a beam splitter results in an accuracy degradation of over 50% in a two-hidden layer fully connected feedforward neural network used for performing MNIST handwritten digit recognition<sup>[22]</sup>. Photonic components that are even more sensitive to fabrication variations are wavelength filters based on interferometers, waveguide gratings or micro-ring resonators. Such devices are used for implementing wavelength division multiplexing (WDM), a workhorse in data center networks<sup>[23–25]</sup>. For spectral photonic filters, a 1 nm deviation in the thickness of waveguides

This article is protected by copyright. All rights reserved.

can result in wavelength shifts of around 1-2 nm which interfere with several communication channels in a dense WDM network<sup>[26]</sup>.

The solution to this problem lies in precisely controlling the optical path length or the effective refractive index of individual components to tailor their output and correct for errors post-fabrication. Prominent techniques accomplish this via active phase shifters using thermo-optic heaters, electro-optic modulators, or micro-electromechanical systems (MEMS) based devices<sup>[27]</sup>. In silicon photonics, modulating the free carrier densities in a diode configuration results in a refractive index change<sup>[28]</sup>. Nevertheless, there are two major drawbacks to active tuning methods: First, a significant part of the power budget is exhausted during operation. Standard CMOS-compatible thermo-optic phase shifters consume around 20 mW for a pi phase shift in a device<sup>[29]</sup>. Scaling this to a wafer scale containing hundreds of thousands of devices is challenging. The second issue is that additional electronic circuitry is required for operation, thus increasing the complexity and footprint of the circuit design. Furthermore, the thermal and electrical crosstalk is also a concern.

Therefore, passive approaches that manipulate the optical properties in a material are an attractive solution. Such approaches include altering either the waveguide or cladding material post-fabrication to obtain a controlled change in the refractive index. Previous work based on electron beam modification of various cladding materials like silicon dioxide (SiO<sub>2</sub>), hydrogen silsesquioxane (HSQ), and polymethyl methacrylate (PMMA) have shown promise in this regard<sup>[30–32]</sup>. However, a major challenge with these approaches is that the wavelength shifts obtained are not stable with time. An alternative approach to tuning the optical properties is by amorphizing crystalline silicon waveguides with Germanium (Ge) ion implantation<sup>[33,34]</sup>. Permanent trimming has been observed in this case but requires local annealing for every device via active components such as thermo-optic heaters. Another

concern is that Ge absorbs light around 1550 nm and 1300 nm wavelength ranges<sup>[35]</sup>, which is the industry standard for fiber optics communications and many other applications. This will induce losses that can be critical, especially for emerging applications in quantum photonics where high-quality factors are desired for performing non-linear operations.

Here, we demonstrate a flexible method for tuning photonic circuits at scale using automated silicon ion implantation in silicon nitride waveguides via marker search and alignment with combined scanning electron microscopy (SEM)-focussed ion beam (FIB) processing, as shown in Fig. 1a. Silicon nitride ( $\text{Si}_3\text{N}_4$ ) is an ultra-low-loss platform and is very well-established in the CMOS industry<sup>[36]</sup>. We obtain controlled and stable shifts in the optical properties without the need for any active elements. Moreover, being mask-less, our approach does not need to be performed at the end of the process flow since there is no need for using a specific cladding material. After performing the tuning operation, further fabrication processes such as the deposition of phase-change materials or electrodes do not affect the circuit. We carry out a detailed material study using scanning transmission electron microscope (STEM) energy-dispersive spectroscopy (EDS) and Electron energy loss spectroscopy (EELS) analysis to understand the fundamental changes occurring at the atomic scale. Leveraging these advances, for the first time, we demonstrate passively aligned energy-efficient photonic circuits enabling applications in wavelength addressable memory and a photonic computing engine exploiting wavelength division multiplexing.

## 2. Results and Discussions

### 2.1. Photonic device tuning

As wavelength selective on-chip components, we use photonic micro-ring resonators. Ring resonators are widely employed in photonic communication systems, sensing, quantum technologies, and optical computing applications<sup>[37]</sup>. What makes them interesting for show-

casing our approach is their sensitivity to fabrication imperfections and environmental conditions. Even slight variations in the geometry of the ring leads to significant shifts in resonance, which can be detrimental to the operation of a given circuit where multiple resonators must be aligned with respect to each other. Whenever the round-trip phase accumulated inside a ring, given by  $2\pi n_{eff}L/\lambda$ , equals multiples of  $2\pi$ , the resonant condition occurs. Here  $n_{eff}$  is the effective refractive index which depends on the geometry of the waveguide and material properties, and  $L$  is the total path length of the ring. Altering the optical path length of the ring translates to shifts in resonances. In our case, the change in optical path length is achieved by creating silicon-implanted regions of increasing length which leads to redshifts in the transmission spectrum as shown schematically in **Figure 1b**. The implantation is carried out using targeted focussed ion beam irradiation at a specific position on the ring, aligned with respect to marker structures fabricated in the vicinity of the resonator. By controlling the length of the implanted region, a desired spectral shift is achieved.

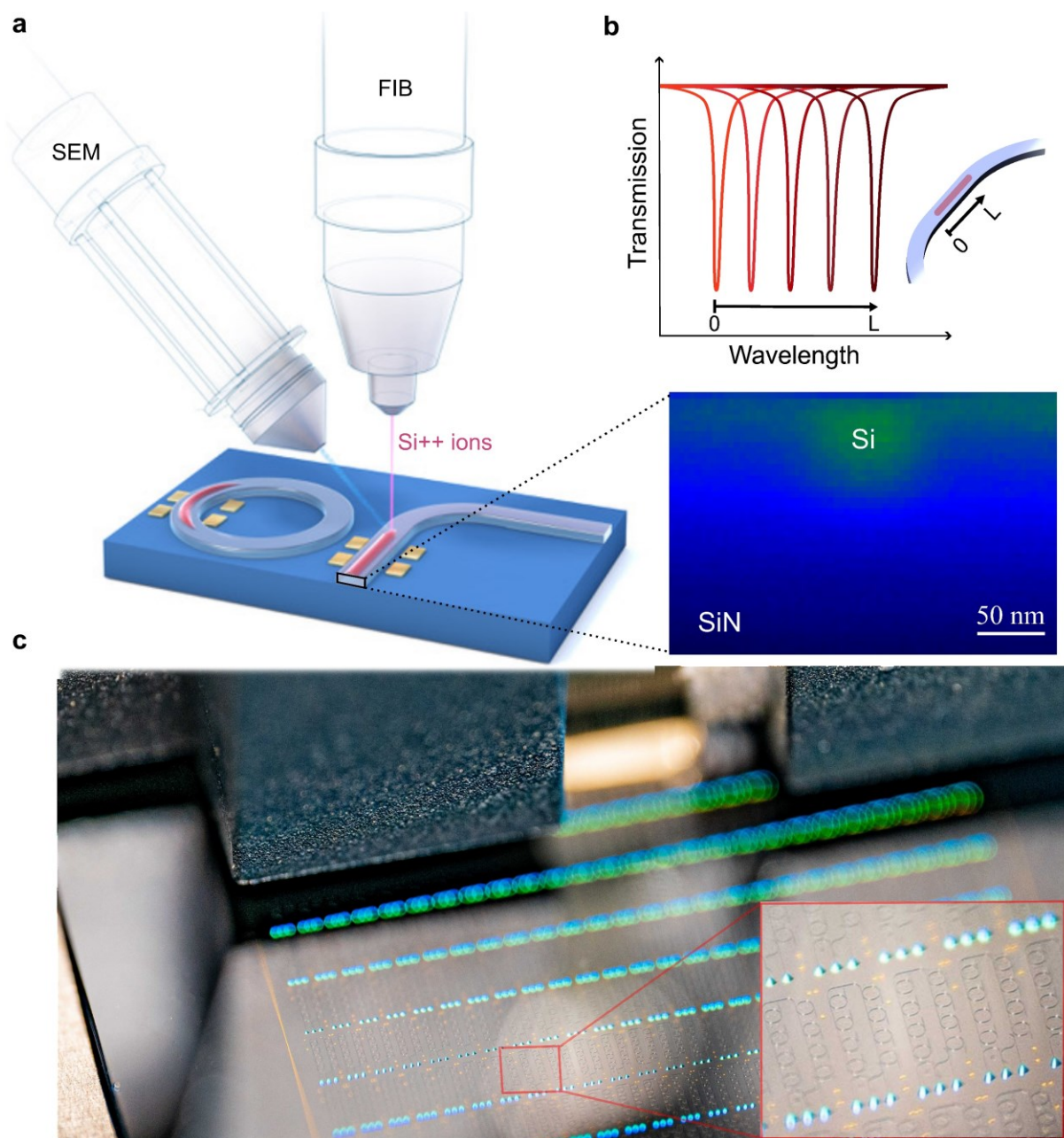


**Figure 1: Photonic device tuning by automatized silicon implantation.** (a) Silicon ion patterning on photonic circuits using the Raith VELION focused ion beam. The photonic circuits consist of silicon nitride ring resonators on top of the  $\text{SiO}_2$  substrate. The ions are directly written into the waveguide without requiring a mask. The inset on the right displays the plasmon map reconstructed from low loss energy spectrum. The patterning process leads to silicon ion implantation in the  $\text{Si}_3\text{N}_4$  waveguides. (b) Schematic of the optical response. Redshifts in the transmission spectrum of ring resonators with larger pattern lengths confirm the increase in the effective refractive index of the waveguide material. (c) A photograph of

the integrated photonic chip showing the scale of the approach. The inset shows a few photonic circuits and gold markers that are used for automatic patterning in the FIB.

## 2.2. Characterizing the material changes

We fabricate  $\text{Si}_3\text{N}_4$  photonic devices with the approach described in the methods section. During FIB implantation of silicon from liquid metal alloy ion sources (LMAIS), a local silicon rich region is created within the waveguide. This is illustrated schematically in the inset of **Figure 1a**. In order to characterize the devices after tuning, we perform a step-by-step analysis of microstructural aspects that are influenced by the implantation process. Upon close examination of the surface morphology in **Figure 2a** the SEM image acquired reveals a discernible line atop the waveguide. Notably, the edges and the core of the line exhibit enhanced brightness in the SEM micrograph, suggesting the presence of silicon or the formation of sharper edges which are favorable sites for the accumulation of electrons.

The subsequent atomic force microscope (AFM) analysis of the surface topography in **Figure 2b** presents evidence that the introduction of Si ions has generated a 15 nm high bump on the surface flanked by distinctively sharper edges on either side. The surface profile is due to a combination of the implantation and sputtering processes that occur simultaneously during FIB processing. In our case, the sputter yield of the target silicon nitride material is very low with a Si ion beam, and the whole process is dominated by the former. The bump shown in the AFM analysis can be attributed to the implantation process which induces stress in the material due to the displacement of atoms. This has been previously shown in amorphous metal ribbons to result in a local free volume expansion<sup>[38]</sup>. Additionally, the sputter process results in the target silicon nitride material getting redeposited on sides of the ion beam path. This is a common phenomenon during ion beam sputtering/milling<sup>[39]</sup>. We expect the sharp edges on either side of the bump to be the gaps between the central bump and redeposited material at the sides.

This article is protected by copyright. All rights reserved.



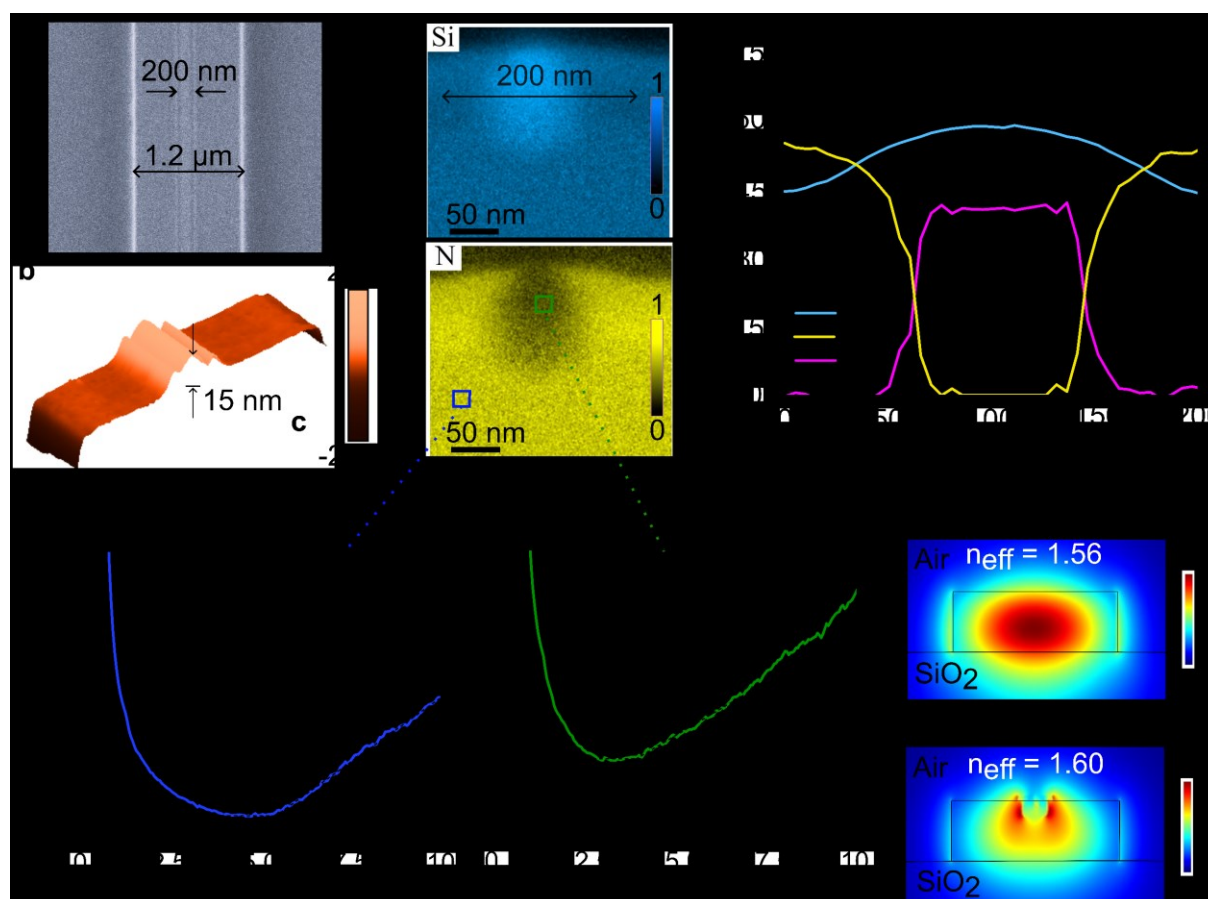


**Figure 2: Material and microstructural analysis:** (a) High-resolution SEM micrograph depicting the intricate surface morphology of the  $\text{Si}_3\text{N}_4$  waveguide after Si implantation. (b) three-dimensional AFM visualization, showcasing the topographic details and revealing a prominent 15 nm elevated protrusion that induces lateral displacement of the  $\text{Si}_3\text{N}_4$  material, thereby introducing additional surface roughness in the vicinity of the Si implantation site. (c) STEM EDS elemental maps, employing a color scale representation, highlighting localized increase in the atomic fraction of Si and suggestive of potential intermixing due to perturbation in the chemical composition of the pristine material. (d) EELS line scans derived from the high-loss signal, providing precise spatial distribution information regarding the constituent elements in the implanted region. It exhibits a discernible presence of silicon and oxygen. (e) Bandgap of the non-implanted waveguide region obtained from EELS plasmon maps. (f) Bandgaps of the implanted region. (g) Simulated fundamental transverse-electric (TE) mode profiles propagating inside the waveguide for bare and implanted configuration showing the contrast in electric-field distribution and effective index.

**Figure 2c** shows the STEM EDS elemental mapping of the  $\text{Si}_3\text{N}_4$  waveguides subjected to patterning. The results indicate a distinguishable and localized increase in the atomic fraction of Si. This presents a high potential for the disruption of existing bonds and the formation of new bonds between the constituent elements of the host material and the implanted Si ions. The implantation profile we observe here also closely matches the ion trajectory simulations (shown in supplementary information section 1).

**Figure 2d** displays the same region, which underwent additional investigation using the EELS elemental mapping. The line scan at the center of implanted region exhibits an increase in Si concentration to 60% and shows a notable presence of oxygen which increases up to 40%. The findings of the EDS analysis are confirmed by this independent technique with complementary information on the local concentration of lighter elements such as nitrogen and oxygen.

The EELS investigation was additionally employed to discern the alterations in the optical characteristics of the  $\text{Si}_3\text{N}_4$  waveguide, as elucidated by the plasmon map in **Figure 1a**. The corresponding bandgap estimations for the pristine waveguide region and the Si implanted region are shown in **Figure 2e** and **Figure 2f**, respectively. An expected decrease in bandgap is observed in the implanted region shifting the absorption edge to higher wavelength of incident photons. The integration of data points acquired from EELS elemental mapping and plasmon mapping facilitated the estimation of the spatial distribution and evolution of the refractive index. This was achieved by constructing a refractive index matrix that captures the intricate distribution and dynamic evolution of the refractive index, arising from the Si ion implantation and localized intermixing of  $\text{Si}_3\text{N}_4$  with Si ions.

We employ this data to perform finite element method (FEM) simulations to estimate the impact of our process on the optical properties at 1550 nm wavelength for a 330 nm high and

1.2  $\mu\text{m}$  wide  $\text{Si}_3\text{N}_4$  waveguide. **Figure 2g** shows that the implantation increases the mode confinement of the fundamental mode, pulling the fields around the implanted region, which results in an increase in the effective refractive index ( $n_{\text{eff}}$ ). The change in the mode profile for the implanted configuration also results in different dispersion characteristics (see **Figure 12** in the supplementary materials). The results suggest that optimising the implantation patterning parameters can be an interesting tool for dispersion engineering. Finally, we use the obtained  $n_{\text{eff}}$  value to analytically calculate the expected resonance shift. This closely matches the measurement results, validating our characterization technique. The detailed analytical calculation for the resonance shifts is provided in the Methods section. Based on this analysis, we can locally tune the optical properties of the waveguide to a desired spectral position after fabrication.

### 2.3. Optical response of the implantation process

Having qualitatively analyzed the material dynamics, we quantitatively assess the process by optical measurements. An exemplary test device with two race-track resonators is shown in **Figure 3a**. The reference ring on the left is used to calibrate the effects of measurement and environmental conditions. We pattern a straight section of the racetrack to standardize the effect of implantation with respect to the length of pattern. The redshift observed in the transmission spectra due to silicon ion implantation can be clearly seen in **Figure 3b**. The inset of this figure plots the spectra in absolute units showing the full-width half maximum (FWHM) which is used to estimate the quality factor (Q) of the rings.

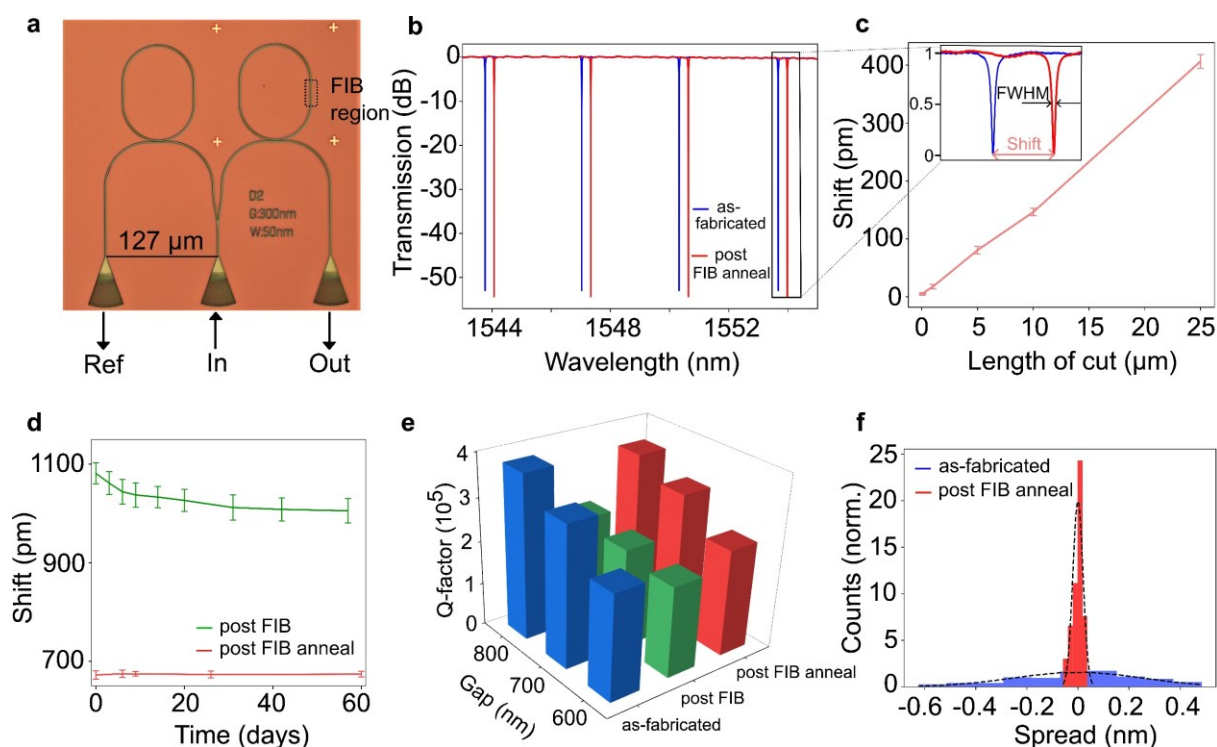


**Figure 3: Spectral alignment through silicon implantation.** (a) Optical micrograph of the device under test used for calibration. The input is split 50/50 to the reference resonator (left) and implanted resonator (right). The gold crosses around the right ring are used for marker detection in the FIB. (b) Transmission spectra before (blue) and after (red) the implantation process. (c) Shifts in resonant wavelengths vs different pattern lengths. Other parameters such as the dose ( $0.1 \text{ nC}/\mu\text{m}^2$ ) and widths (50 nm) are constant. A total of 10 devices per pattern length is used for the tests. (d) Stability of shifts. Annealing the sample after the implantation process stabilizes the shifts and also improves the standard deviation as shown in the red curve. (e) Study of losses induced due to implantation. All the devices are patterned with the same parameters. The quality factors are retained after annealing even for larger gaps. (f) Statistics of the implantation process. The resonance spread of 100 rings spanning the length of our chip is shown before (blue) and after (red) tuning. The area under the histogram is normalized to 1 for both cases.

**Figure 3c** shows the deterministic relationship between the shift in resonances and the pattern length of the implanted region. While keeping the dose of the ion beam constant, a linear relationship between the length of the pattern and shift is obtained. Here, a shift ranging from  $6 \pm 1 \text{ pm}$  to  $400 \pm 10 \text{ pm}$  is observed for lengths ranging from 100 nm to 25 μm. Larger shifts in the nm range can also be produced by using higher doses or larger widths

This article is protected by copyright. All rights reserved.

(shown in supplementary information section 2). The stability of the induced shifts with time under ambient environmental conditions is shown in **Figure 3d**. After patterning, as depicted in the green curve, the shift starts to decay with time because the implantation process creates defects and impurities which are prone to chemical reactions in the atmosphere. This was confirmed with EELS elemental maps, where the post-FIB sample was heavily contaminated. However, annealing the sample in a tube furnace after FIB writing aids in thermal diffusion and removes the ion-induced damage. The heat treatment not only facilitates the relaxation of  $\text{Si}_3\text{N}_4$  following Si implantation, but also engenders an additional oxidation process within the confines of the tube furnace (more details in Table 1 supplementary).

This oxidative transformation effectively lowers the surface energy by the formation of new chemical bonds, thereby contributing to the enhanced stability and robustness of the material. We observe a blue shift immediately after annealing as shown in the red curve which remain constant afterwards. The stability tests were performed by leaving the chip in ambient conditions with exposure to different temperatures, air pressure, humidity and presence of dust particles. The shifts obtained also show stability after performing further lithography and deposition steps. We also found that further annealing steps on the same chip do not impact the stability of the already tuned devices. This characteristic is especially crucial in making the implanted devices compatible within a packaged circuit that could be subject to elevated operational temperatures due to neighbouring electronics.

Next, we analyse the optical loss induced during the implantation process by comparing Q-factors before and after tuning. The Q-factor is inversely proportional to the power loss per round trip. High Qs in the order of  $10^5$  and  $10^6$  are desired for obtaining strong non-linear interactions for applications such as generating entangled photons. By increasing the gap between the bus waveguide (used for probing light in and out) and the ring, the ring resonator

can be moved from an over-coupling to an under-coupling regime. This increases the lifetime of a photon inside the ring and results in high  $Q$ s (more details are presented in supplementary information section 2). In **Figure 3e**, the change in the  $Q$ -factor due to the implantation process is shown. As the  $Q$  value of the intrinsic resonator gets higher, patterning with the same dose and size leads to a larger loss. Nevertheless, annealing the sample post-FIB recovers the  $Q$  values to around half a million. This result is also consistent with the findings concerning annealing described above.

By extrapolating the measured  $Q$  values to the weakly-coupled case, the propagation losses are determined and shown in **Table 1**. The loss values are given for a dose of  $0.1 \text{ nC}/\mu\text{m}^2$  which is used for obtaining the shifts in **Figure 3**. These values can be further reduced by decreasing the dose which will reduce the reflections at the interface between as fabricated and implanted regions, assumed to be the main contribution to the loss induced through our process. Furthermore, patterning the entire racetrack or introducing a taper before and after the implanted section can also minimise the losses enabling adiabatic mode transition. With a reduced dose, higher shifts can still be obtained by increasing the length of the pattern.

as-fabricated [dB/cm]	post FIB [dB/cm]	post FIB anneal [dB/cm]
0.88	1.43	0.95

**Table 1:** Extracted propagation losses in the waveguide

To analyze the reproducibility of our approach, **Figure 3f** depicts statistics collected from ring resonator tuning. The blue histogram shows the resonance spread after fabrication for 100 rings identical in design. The red curve shows the spread in resonances for identical FIB patterns designed to perform a coarse tuning operation. Here, the standard deviation of the target resonance for 100 rings is reduced to 20 pm. In order to achieve even higher precision,

coarse tuning can be followed up with a fine-tuning operation which as shown in **Figure 3b** can be used to achieve sub-10 pm accuracy. This is employed in the applications described in the following section.

#### 2.4. Wavelength-addressable optical memory

As a first example, we demonstrate an optical memory architecture shown in **Figure 4a** using multiple add-drop ring resonators combined with functional materials. Here, we store information in the light's amplitude that is modulated through evanescent interaction with phase-change material (PCM). We use the ternary alloy  $\text{Ge}_2\text{Sb}_2\text{Te}_5$  (GST) well-known for its non-volatile memory functionality. For GST, a change in the structure from amorphous to crystalline state leads to an increase in the absorption coefficient which is exploited for realizing a multi-level memory<sup>[15,40]</sup>. This functionality has also been used to store matrix weights and perform energy efficient optical in-memory computing<sup>[12,16]</sup>.

Our device architecture consists of 8 unit cells, each functioning as a photonic memory which is addressed with a unique wavelength. Within one unit cell, a ring resonator is used to filter specific wavelengths of light. The resonator is connected to a PCM cell that stores information and a Bragg filter which is designed to reflect the incoming light to achieve higher memory depth in a double pass (**Figure 4b**). This architecture results in a very compact design where the input and output light travels in opposite directions, as shown by the dotted lines (**Figure 4a**). Each ring is designed to operate at separate wavelengths so that all the rings can be accessed simultaneously. The design details of the Bragg filter and memory architecture is given in supplementary information section 3.

For practical purposes, it is crucial that multiple memory blocks show the same resonance spectra. Otherwise, addressing each device would require 8 unique wavelengths for a fast

parallel operation making scalable operation very challenging. Moreover, the scalability could be further improved by designing the resonances equidistant so that a single-frequency comb source can be used for read and write access<sup>[41]</sup>. In the upper panel of **Figure 4c**, we show the transmission spectra of two memory blocks that were designed to have the same equidistant resonances. Before the tuning operation, the spectra are not aligned and show wavelength offsets. Using our implantation process, we correct for the deviations and align the spectra to be equidistant with 300 pm spacing, as shown in the lower panel.

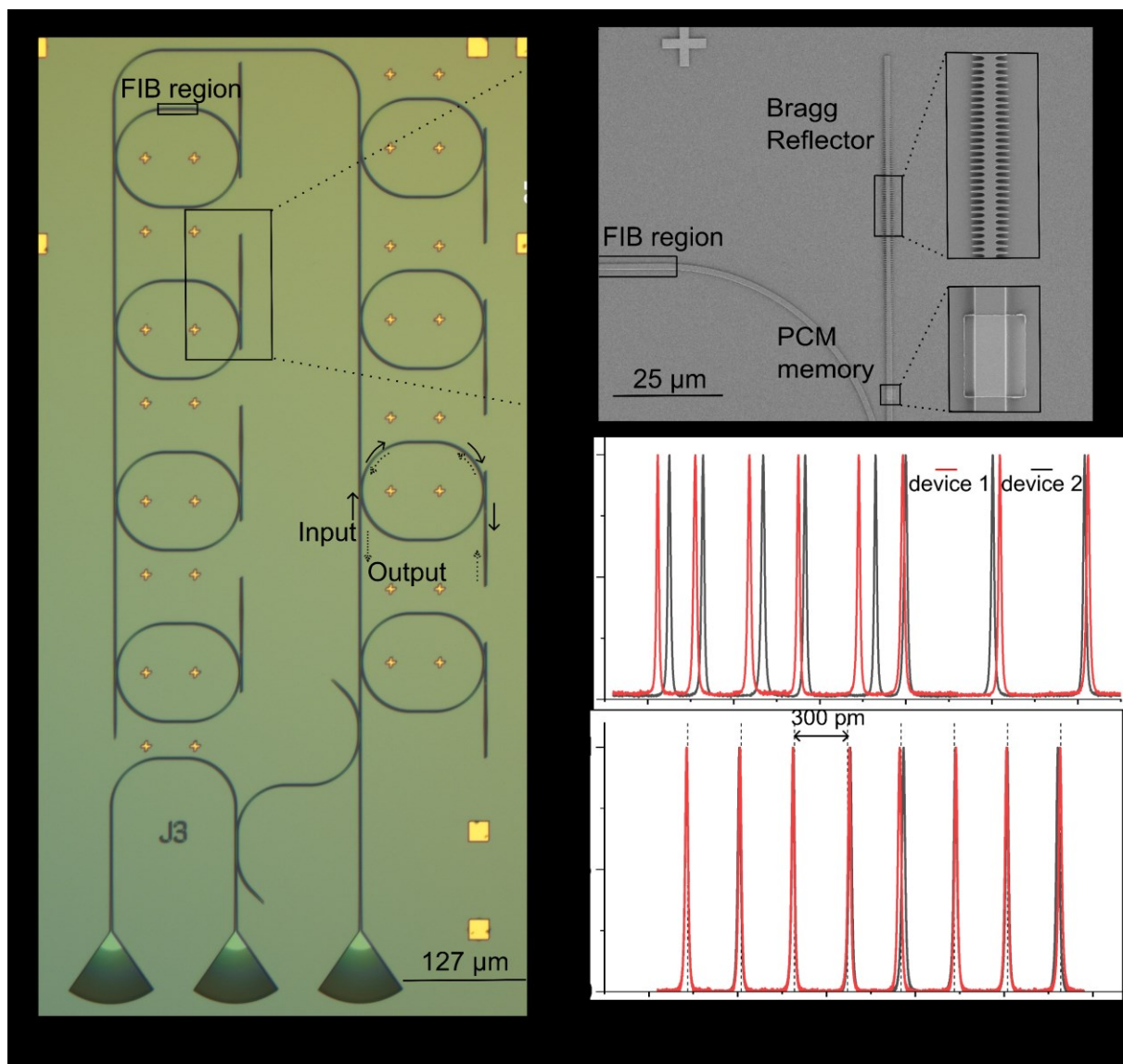


**Figure 4: Wavelength addressable photonic memory.** (a) Optical micrograph of one memory block that can store up to 8 analog values. The combination of a ring, PCM memory,



and Bragg filter act as a unit cell. The solid and dotted arrows trace the path of the light for one unit cell showing the input and output respectively. (b) Mechanism of memory storage in a unit cell. Light couples from the ring to the adjacent waveguide where it interacts with a PCM cell that modulates its intensity. After this interaction, the light gets reflected using a Bragg grating, interacts again with the PCM cell, and couples back into the ring for the readout. (c) Transmission spectrum of two devices after device fabrication (upper panel) and post-FIB tuning (lower panel).

## 2.5. Photonic computing for accelerated General-Matrix Multiplications (GEMM)

As a second example, we explore a photonic computing architecture using ring resonators for wavelength division multiplexing. Modern data centers employ electronic hardware like graphical processing units (GPU)s and tensor processing units (TPU)s for performing arithmetic tasks such as neural network inferencing. Most of their processing time is spent performing mathematical operations in parallel, i.e., matrix-vector multiplications<sup>[42]</sup>. This has led to a lot of interest in the community to develop specialized matrix multiplication hardware for accelerating artificial intelligence (AI) workloads<sup>[43,44]</sup>. Photonic solutions have shown great promise lately<sup>[12,45]</sup> and may complement conventional products in many AI applications. Ring resonator-based configurations are particularly attractive<sup>[46–48]</sup> since they show non-linear behaviour and can be used as multiplexers or demultiplexers inside the circuit allowing for a compact, loss-less, and parallel operation on several wavelengths. However, still plagued by the uncertainties induced due to fabrication, all photonic computing implementations until now have relied on active methods to perform the correction.

Here, we employ a photonic circuit comprising of passively tuned ring resonators to carry out matrix-vector multiplications in parallel (**Figure 5a**). We perform convolution operations as used in computer vision for edge detection within an input image. The input image data is

encoded in the amplitude of the incoming light. This is done using an electro-optic modulator (EOM) for each channel to the matrix. The EOMs are controlled using an external field programmable gate array (FPGA) that sends the input image pixel data at a 2 GHz clock frequency. Once the pixel information is encoded in the input light intensities, they are passed on to the matrix for the multiplication and accumulation operation. We operate in a weight-stationary inference scheme where the kernels are flattened and loaded in the state of the phase-change material (GST cell). At the output of each column, the convolved image data is obtained for that individual kernel.

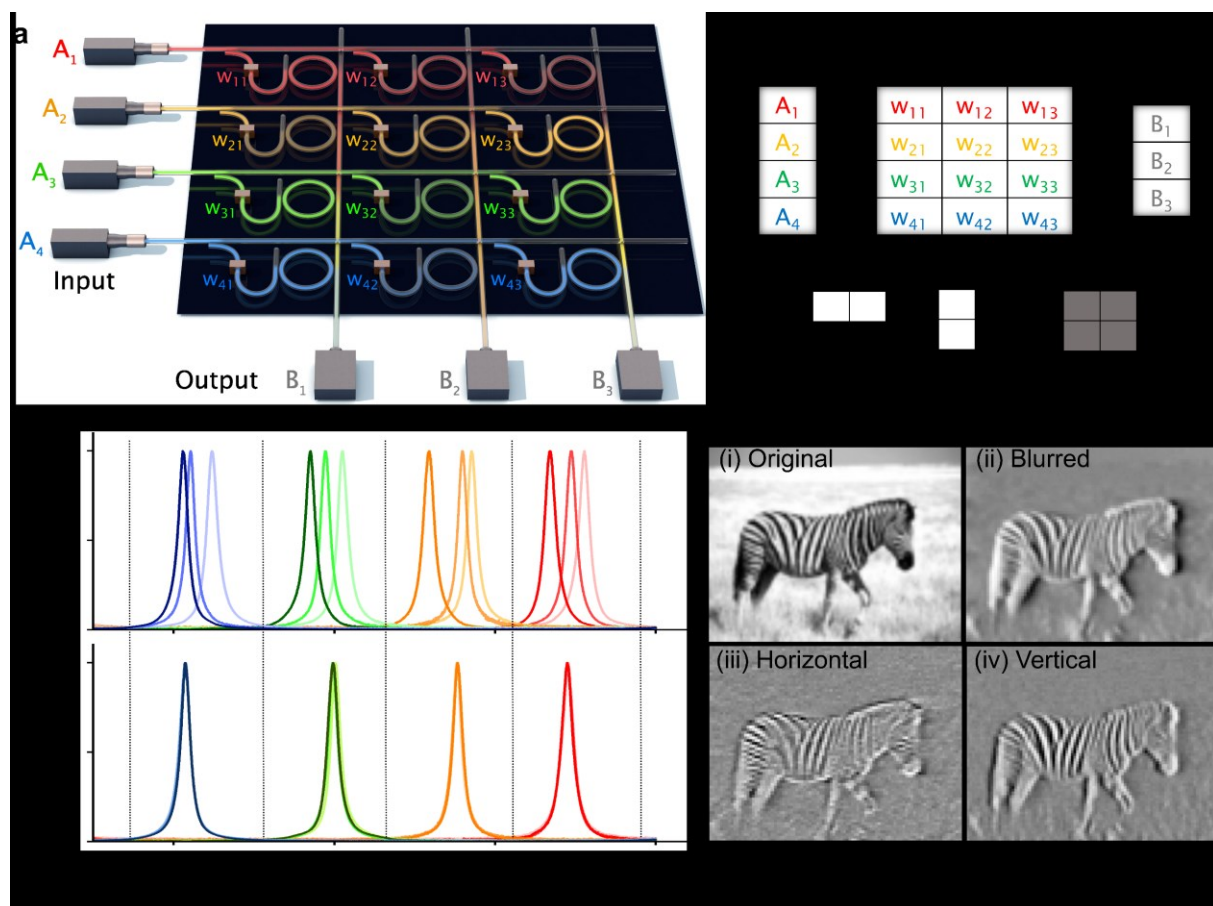


**Figure 5: Matrix vector multiplication architecture for edge detection.** (a) Schematic of a 4X3 matrix multiplication circuit. An input image vector that needs to be inferred is encoded in the amplitude of incoming light to the matrix. Each element of the vector is encoded in a unique wavelength for parallel processing. Directional couplers are used to split equal intensities of light from the rows to the PCM cells that store the weights of the network. Ring

This article is protected by copyright. All rights reserved.

resonators are used to finally couple the light into the columns. For the ideal configuration, the three resonators in each row are designed to be aligned at the same wavelengths as illustrated inside the color coding of the schematic. (b) Transmission spectrum of the circuit right after fabrication (upper panel); and after post-fabrication tuning (lower panel). (c) Edge detection example. The grayscale zebra image shown in (i) is sent as the input; (ii), (iii), and (iv) show the output computed for respective filters.

Using ring resonators in this photonic circuit allows us to encode the four elements of the input vector in separate wavelengths with none of the rows interacting with one other. This results in negligible additional loss while scaling the rows of the matrix. However, a key requirement is that all three rings in each row need to have the same wavelength for accessing the three kernels simultaneously. This is not the case after fabrication as shown in the upper panel of **Figure 5b**. Each row in our case is misaligned by around 100-400 pm. These errors are measured and corrected automatically in the FIB using the calibration data. The result is shown in the lower panel of **Figure 5b**, where all the resonances are perfectly aligned. After the tuning operation, we carry out the phase-change material (PCM) deposition. The PCM cells are switched optically to store the flattened kernel data. The optical micrograph and SEM pictures of the fabricated circuit are shown in the supplementary information section 3.

Finally, the convolved output is measured using photodetectors at the end of each column. The obtained currents are sent back to the FPGA where the output image is reconstructed. **Figure 5c** shows the output of three kernels convolved on the test zebra image shown in (i). A blurred output (obtained by using a kernel to implement photonic low-pass filtering) is shown in (ii), whereas (iii) and (iv) show the results of implementing photonic edge-detection in the horizontal and vertical directions respectively.

### 3. Conclusions

This article is protected by copyright. All rights reserved.

We have demonstrated a scalable, robust, and low loss method for precisely controlling the optical path lengths in silicon nitride photonic integrated circuit devices. The method can be used to effectively correct the random inaccuracies that occur during fabrication in an automated process. We also demonstrated the ability for precise spectral alignment of resonances (e.g., to a micro-comb source), and implemented such a system in a passive ring-resonator-based photonic matrix multiplication circuit. If we assume the fabrication error in the resonance wavelength to be 30% of the free spectral range (FSR) (a value based on our measured statistics), and 20 mW power required to tune over the whole FSR (for a conventional thermo-optic phase shifter<sup>[29]</sup>), we save around 6.66 mW per each resonator compared to an active approach. For our proof of principle matrix multiplication circuit, this accounts to be approximately 60 mW reduction in the power budget. For commercial applications that aim for larger matrix sizes such as 128x128, the power budget savings quickly scale to upwards of 100 W, a very important and significant improvement in energy efficiency. Similar parallels can be drawn for optical I/O technologies in which a high bandwidth transceiver module can contain up to 8 ring modulators whose transmission spectrum needs to fit WDM schemes. We can readily obtain such spectrums using our implantation method, as we showed in the photonic memory application.

The fact that our process is maskless also allows for further fabrication steps after tuning. We also demonstrated that our approach is robust to temperature and environmental changes. We show that the losses induced due to the ion implantation process are negligible, with high Qs of around half a million. This is crucial for some applications such as photonic quantum computers that demand ultralow losses. We demonstrated the capabilities of our tuning approach via modification of transmission spectra in ring resonator devices, but our process is applicable to other key integrated photonic components such as beam splitters,

interferometers, or directional couplers. Indeed, since all of these components are less sensitive than a ring resonator to changes in effective index, our approach will be very well suited to the correction of fabrication tolerances in them. Finally, we point out that our scheme of changing the optical properties using a silicon ion FIB is not just limited to silicon nitride waveguides and could also be translated to other integrated photonics material platforms such as Silicon-On-Insulator or Lithium-Niobate-On-Insulator.

#### 4. Methods

##### *Device fabrication*

The photonic circuits used in this study are designed using gdshelpers<sup>[49]</sup>, a Python-based open-source design framework for integrated circuits. The material stack we use is stoichiometric low pressure chemical vapor deposited (LPCVD)  $\text{Si}_3\text{N}_4$  films (330 nm) on top of  $\text{SiO}_2$  dielectric (3300 nm) with Silicon as the substrate material. The cladding on top is air. The wafers are acquired from Rogue Valley Microdevices. Our process flow consists of three steps, first is to write the gold markers required for later steps. In the second step, we pattern the photonics. The phase-change material (GST) patterning is done at last.

For the gold markers, we start with spin-coating the positive photoresist polymethyl methacrylate (PMMA) from AllResist AR-P 672 series. After baking the resist, a 100kV electron beam lithography tool (Raith EBPG 5150) is used to expose the marker regions. Next, the chip is developed in a methyl isobutyl ketone (MIBK) and isopropyl alcohol (IPA) solution. Following this, a stack of chromium (5nm) / gold (80 nm thick) / chromium (5nm) is deposited on the chip using physical vapor deposition (PVD). The chromium on the bottom and top is used for better adhesion and protection of the gold surface. Lastly, the liftoff process of the resist is undergone in acetone to get the final markers. For the next two steps, these markers are used for alignment.

This article is protected by copyright. All rights reserved.

We write photonics using a negative resist (AR-N 7520 series) that is spin-coated for obtaining a thickness of 350 nm. The waveguide regions are then exposed using the electron beam with small currents and step sizes to obtain high accuracy. After developing this chip in the Microposit MF-319 solution, we have the mask ready for etching. This is done using a Reactive Ion Etching tool from Oxford Instruments. We use a plasma consisting of CHF<sub>3</sub> and O<sub>2</sub> to etch the un-exposed silicon nitride regions. The last step is to strip the resist using oxygen plasma.

For patterning GST, we follow the same steps as for the gold. We expose the PMMA resist in regions where the phase-change material is desired. After development, we sputter 10 nm GST on top of our chip and a 10 nm layer of ITO as a protective layer on top. Finally, acetone is used to liftoff the resist.

#### *Post-fabrication tuning*

We use the Raith VELION FIB<sup>[50]</sup>, that is capable to provide various ion species from liquid metal alloy ion sources (LMAIS), to tune the refractive index of silicon nitride waveguides. A 35 kV Si<sup>++</sup> beam with an aperture size of 30 μm is selected for the implantation process. The patterns that need to be written using the FIB are set on a separate layer in a GDSII design file, which is the industry standard for IC layout. This file is loaded into the FIB and patterning is carried out using marker alignment in a maskless process. Post-FIB, the samples are annealed in a tube furnace at 400 °C for two hours to stabilize the shifts.

For tuning the photonic circuits, the fabrication deviations are measured in an automatic measurement setup. The shifts required for aligning everything are then mapped to the length of the FIB pattern using calibration data (similar to **Figure 3c**). Finally, this design is loaded into the FIB, and the rings are aligned in a fully automated process.

### *Microscopy and sample preparation*

The Si<sub>3</sub>N<sub>4</sub> waveguides were further analyzed in the as-fabricated and implanted states using a TEM. Prior to the TEM microscopy, thin lamellae were prepared from the regions of interest using the FIB technique in a ZEISS Crossbeam 340 SEM/FIB. Thereafter, these prepared thin samples were studied using a Titan Themis G3 300 TEM (FEI) microscope operated in STEM mode. Elemental mapping was performed using element-dispersive spectroscopy (EDS) with a quadrupole EDX system, and a high-angle annular dark-field (HAADF) detector (Fischione Model 3000). The high brightness field emission gun (X-FEG) in this microscope is operated at 3.45 kV extraction voltage and 300 kV acceleration voltage, along with a monochromator. EELS was performed in STEM mode at 60 kV in the form of spectrum imaging using a Quantum 965 ER Gatan imaging filter (GIF). The following experimental parameters were used: a probe size of 0.5 nm, a beam current of 36 pA, an energy resolution of 0.5 eV, an energy dispersion of 0.05 eV/channel, a convergence semi-angle of 22 mrad, a collection semi-angle of 10 mrad acquiring EELS spectra with 40 ms dwell-time subsequently integrating over 5 frames.

### *Numerical analysis and simulations*

The mode profiles are simulated using Lumerical Mode, a Finite-Difference Eigenmode solver. We model the silicon implantation region by a map of coefficients that contain the composition of Si<sub>3</sub>N<sub>4</sub> and Si for each pixel. This coefficient map is acquired from EELS elemental mapping and plasmon mapping. We finally obtain the wavelength dependent refractive indices of the implanted region by taking a weighted sum of these coefficients. The material dispersion data for Si and Si<sub>3</sub>N<sub>4</sub> used in these calculations is fitted to the Sellmeier equation<sup>[51,52]</sup>. For the mesh settings, we use a combination of graded and conformal meshing available in Lumerical. The implanted region has a finer mesh with a maximum mesh size of

10 nm. The simulation region is large enough such that the evanescent fields decay completely leading to minimal reflections. We use metal boundary conditions for the simulation region.

After solving the Maxwell's equations on a cross-sectional mesh of the waveguide, the solver returns the mode profile and effective index of the fundamental TE mode. Plugging in the effective index into the formulae  $2\pi n_{\text{eff}}L = m\lambda$ , the shift in wavelength can be calculated. In the formula above,  $n_{\text{eff}}L$  is a combination of the implanted straight section and the rest as-fabricated racetrack. For the case shown in **Figure 2** of the main text, the calculated shift is 2.7 nm for a 50  $\mu\text{m}$  ring radius and two 25  $\mu\text{m}$  straight sections (one of which is implanted with 200 nm pattern width and 0.8  $\text{nC}/\mu\text{m}^2$  dose). This is in concurrence with the experimental data shown in **Figure 11** supplementary, where shifts up to 2 nm can be observed for a similar patterning width.

For the simulation of the Bragg cavities, we perform it using Lumerical's variational finite-difference time-domain (var FDTD) solver. We inject the fundamental TE mode source through the input and study the transmission, reflection, and electric-field propagation along the cavity.

#### *Measurement setup*

For the optical characterization experiments shown in **Figure 3**, we use a simple scheme consisting of a tunable laser source (Santec TSL-710), a polarization controller, a fiber array, and a photodetector (Newport Model 2011). The chip is placed on top of a vacuum-enabled stage that can be controlled through piezo motors via a closed-loop algorithm enabling sub-micron precision. Using this, we automate our measurement process in such a way that the stage moves under the fiber array to the next region of interest, optimizes the transmission,



performs wavelength sweep, and saves the data. A schematic of this setup is shown in supplementary information section 2.

Here, light is coupled in and out of our chip using grating couplers. For calculating the shifts, we study the difference between the output resonance positions and reference resonance positions before and after patterning (**Figure 3a**). In this way, we negate the effect of environmental and measurement conditions. In the memory application shown in **Figure 4**, we use a commercially available gas reference cell (HCN) for calibrating the wavelengths precisely.

In the convolution measurement (**Figure 5**), we use a CW laser source as input for each row. It emits light at the specific wavelength that row is designed for operation. Next, the light is intensity-modulated using an analog electro-optic modulator (EOMs) from Optilab whose 3 dB bandwidth is 30 GHz. Using, this we generate pulses with each pulse encoding a pixel value from the input. The EOMs are controlled electrically using an FPGA, that stores the input image digitally. This image is fragmented according to the kernel size and passed on to a digital-to-analog converter (DAC) and sent to the EOM for encoding the data in light intensities. We couple this light into our chip using a fiber array and grating couplers like the setup mentioned before. The matrix multiply and accumulate operations for all three kernels take place parallelly on-chip at the speed of light. The output for each kernel is measured at the end using photodetectors from Thorlabs that can go up to 10 GHz. The detected photocurrents are sent to the analog to digital converters (ADCs) on the FPGA and the convoluted images are reconstructed. The entire convolution operation is performed at a fast clock rate of 2 GHz, limited only by electronic components such as DACs and ADCs. A schematic of the setup is shown in supplementary information section 3.

### *Statistical Analysis*

This article is protected by copyright. All rights reserved.

The bandgap data in **Figure 2e** and **Figure 2f** is obtained by taking the intersection from the horizontal background level and the curve obtained by linear fitting the low loss spectrum. This was performed in the DigitalMicrograph software from Gatan. The error bars in **Figure 3c** and **Figure 3d** indicate the standard deviation for each parameter. We use a total of 10 devices per pattern length in the **Figure 3c**. The stability test (**Figure 3d**) is shown for 20 devices that were patterned with the same length and dose. There are no outliers in the data. The Q-factor data in **Figure 3e** is obtained by fitting each transmission spectra to a perfect Lorentzian fit (R-squared of 100%). The histogram data in **Figure 3f** is normalized such that the area under the histogram is 1 for both the as-fabricated and post-FIB annealed case. The total number of samples for the histogram data is 100. These devices span the entire length of the 15 mm chip. The transmission spectra shown in **Figure 4c** and **Figure 5b** are normalized to one.

### Acknowledgements

F.B.P., and W.H.P.P acknowledges support from the Volkswagen Foundation. W.H.P.P. acknowledges support by the European Research Council (ERC, PINQS Project). We thank Jochen Stuhmann for assistance with the graphical illustrations and Jonas Schütte with the optical images. This work was supported by the European Union's Horizon 2020 research and innovation programme (grant no. 101017237, PHOENICS Project) and the European Union's Innovation Council Pathfinder programme (grant no. 101046878, HYBRAIN Project). We acknowledge funding support by the Deutsche Forschungsgemeinschaft (DFG, German Research Foundation) under Germany's Excellence Strategy EXC 2181/1 – 390900948 (the Heidelberg STRUCTURES Excellence Cluster), the Excellence Cluster 3D Matter Made to Order (EXC-2082/1—390761711) and CRC 1459 “Intelligent matter”.

### Author contribution

This article is protected by copyright. All rights reserved.

AV, FBP and ST performed the experiments with assistance from IB and DB. HR and ST performed the TEM analysis. MK assisted in the TEM sample preparation. AV and DB performed the Si implantation with assistance from TR and AN. All authors analyzed the data and wrote the manuscript.

### Competing interests

The authors declare no competing interests.

### Data Availability Statement

All data used in this study are available from the corresponding author upon reasonable request.

### References

- [1] D. Amodei, D. Hernandez, “AI and Compute,” can be found under <https://openai.com/research/ai-and-compute>, accessed: September **2023**.
- [2] “How the way we compute is changing”, editorial, *Nat Electron* **2023**, 6, 329.
- [3] B. J. Shastri, A. N. Tait, T. Ferreira de Lima, W. H. P. Pernice, H. Bhaskaran, C. D. Wright, P. R. Prucnal, *Nat Photonics* **2021**, 15, 102.
- [4] C. Demirkiran, F. Eris, G. Wang, J. Elmhurst, N. Moore, N. C. Harris, A. Basumallik, V. J. Reddi, A. Joshi, D. Bunandar, *ACM J Emerg Technol Comput Syst* **2023**, 19, 1.
- [5] A. Sludds, S. Bandyopadhyay, Z. Chen, Z. Zhong, J. Cochrane, L. Bernstein, D. Bunandar, P. Ben Dixon, S. A. Hamilton, M. Streshinsky, A. Novack, T. Baehr-Jones, M. Hochberg, M. Ghobadi, R. Hamerly, D. Englund, *Science (1979)* **2022**, 378, 270.
- [6] L. S. Madsen, F. Laudenbach, M. Falamarzi. Askarani, F. Rortais, T. Vincent, J. F. F. Bulmer, F. M. Miatto, L. Neuhaus, L. G. Helt, M. J. Collins, A. E. Lita, T. Gerrits, S.

This article is protected by copyright. All rights reserved.

- W. Nam, V. D. Vaidya, M. Menotti, I. Dhand, Z. Vernon, N. Quesada, J. Lavoie, *Nature* **2022**, 606, 75.
- [7] M. Butcher, “This startup hopes photonics will get us to AI systems faster,” can be found under <https://techcrunch.com/2022/05/12/this-startup-hopes-photonics-to-will-get-us-to-ai-systems-faster/>, accessed: September **2023**.
- [8] “PsiQuantum Will Partner with DARPA to Accelerate Path to Build the World’s First Utility-Scale Quantum Computer,” can be found under <https://psiquantum.com/news/psiquantum-will-partner-with-darpa-to-accelerate-path-to-build-the-worlds-first-utility-scale-quantum-computer>, accessed: September **2023**.
- [9] “Xanadu closes \$100M USD Series C to accelerate development of fault-tolerant quantum computers,” can be found under <https://xanadu.ai/press/xanadu-closes-100M-USD-series-c-to-accelerate-development-of-fault-tolerant-quantum-computers>, accessed: September **2023**.
- [10] T. Weiland, “Celestial AI, the Creator of the Photonic Fabric Optical Interconnect Technology Platform, Raises \$100 Million in Series B Funding,” can be found under <https://www.businesswire.com/news/home/20230627995436/en/Celestial-AI-the-Creator-of-the-Photonic-Fabric-Optical-Interconnect-Technology-Platform-Raises-100-Million-in-Series-B-Funding>, accessed: September **2023**.
- [11] Y. Shen, N. C. Harris, S. Skirlo, M. Prabhu, T. Baehr-Jones, M. Hochberg, X. Sun, S. Zhao, H. Larochelle, D. Englund, M. Soljačić, *Nat Photonics* **2017**, 11, 441.
- [12] J. Feldmann, N. Youngblood, M. Karpov, H. Gehring, X. Li, M. Stappers, M. Le Gallo, X. Fu, A. Lukashchuk, A. S. Raja, J. Liu, C. D. Wright, A. Sebastian, T. J. Kippenberg, W. H. P. Pernice, H. Bhaskaran, *Nature* **2021**, 589, 52.

- [13] L. Liao, S. Fatholouloumi, K. Nguyen, H. Mahalingam, D. Hui, J. Heck, H. Frish, R. Defrees, C. Malouin, P. Seddighian, M. Huang, K. Al-hemyari, Y.-J. Chen, Y. Wang, W. Lin, D. Zhu, R. Jones, Y. Akulova, T. Liljeberg, in *Optical Fiber Communication Conference (OFC) 2023*, Optica Publishing Group, San Diego California, **2023**, p. Th3B.1.
- [14] A. Rizzo, A. Novick, V. Gopal, B. Y. Kim, X. Ji, S. Daudlin, Y. Okawachi, Q. Cheng, M. Lipson, A. L. Gaeta, K. Bergman, *Nat Photonics* **2023**, *17*, 781.
- [15] C. Ríos, M. Stegmaier, P. Hosseini, D. Wang, T. Scherer, C. D. Wright, H. Bhaskaran, W. H. P. Pernice, *Nat Photonics* **2015**, *9*, 725.
- [16] C. Ríos, N. Youngblood, Z. Cheng, M. Le Gallo, W. H. P. Pernice, C. D. Wright, A. Sebastian, H. Bhaskaran, *Sci Adv* **2019**, *5*, eaau5759.
- [17] R. Chen, Z. Fang, C. Perez, F. Miller, K. Kumari, A. Saxena, J. Zheng, S. J. Geiger, K. E. Goodson, A. Majumdar, *Nat Commun* **2023**, *14*, 3465.
- [18] Y. Xing, J. Dong, U. Khan, W. Bogaerts, *ACS Photonics* **2023**, *10*, 928.
- [19] M. Santandrea, M. Stefszky, V. Ansari, C. Silberhorn, *New J Phys* **2019**, *21*, 033038.
- [20] A. Prinzen, M. Waldow, H. Kurz, *Opt Express* **2013**, *21*, 17212.
- [21] J. Pond, G. S. C. Lamant, R. Goldman, in *Optical Fiber Telecommunications VII* (Ed.: A. E. Willner), Academic Press, **2020**, pp. 195–231.
- [22] M. Y.-S. Fang, S. Manipatruni, C. Wierzynski, A. Khosrowshahi, M. R. DeWeese, *Opt Express* **2019**, *27*, 14009.

- [23] C. Levy, Z. Xuan, D. Huang, R. Kumar, J. Sharma, T. Kim, C. Ma, G.-L. Su, S. Liu, J. Kim, X. Wu, G. Balamurugan, H. Rong, J. Jaussi, in *2023 IEEE Custom Integrated Circuits Conference (CICC)*, **2023**, pp. 1–2.
- [24] A. Chakravarty, K. Schmidtke, V. Zeng, S. Giridharan, C. Deal, R. Niazmand, in *Frontiers in Optics 2017*, OSA, Washington, D.C., **2017**.
- [25] D. J. Blumenthal, H. Ballani, R. O. Behunin, J. E. Bowers, P. Costa, D. Lenoski, P. A. Morton, S. B. Papp, P. T. Rakich, *Journal of Lightwave Technology* **2020**, *38*, 3376.
- [26] W. Bogaerts, S. K. Selvaraja, P. Dumon, J. Brouckaert, K. De Vos, D. Van Thourhout, R. Baets, *IEEE Journal of Selected Topics in Quantum Electronics* **2010**, *16*, 33.
- [27] K. Padmaraju, K. Bergman, *Nanophotonics* **2014**, *3*, 269.
- [28] R. Soref, B. Bennett, *IEEE J Quantum Electron* **1987**, *23*, 123.
- [29] S. Liu, J. Feng, Y. Tian, H. Zhao, L. Jin, B. Ouyang, J. Zhu, J. Guo, *Frontiers of Optoelectronics* **2022**, *15*, 9.
- [30] J. Schrauwen, D. Van Thourhout, R. Baets, *Opt Express* **2008**, *16*, 3738.
- [31] L. Thiel, A. D. Logan, S. Chakravarthi, S. Shree, K. Hestroffer, F. Hatami, K.-M. C. Fu, *Opt Express* **2022**, *30*, 6921.
- [32] N. Farmakidis, H. Yu, J. S. Lee, J. Feldmann, M. Wang, Y. He, S. Aggarwal, B. Dong, W. H. P. Pernice, H. Bhaskaran, *Nano Lett* **2023**, *23*, 4800.
- [33] M. M. Milosevic, X. Chen, W. Cao, A. F. J. Runge, Y. Franz, C. G. Littlejohns, S. Mailis, A. C. Peacock, D. J. Thomson, G. T. Reed, *IEEE Journal of Selected Topics in Quantum Electronics* **2018**, *24*, 1.

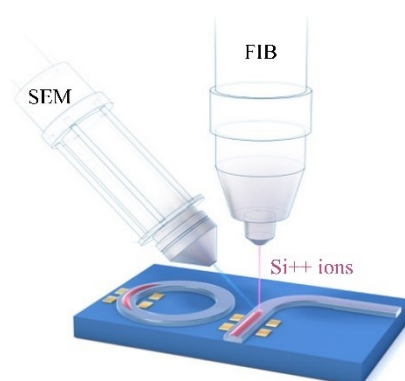
- [34] H. Jayatilleka, H. Frish, R. Kumar, J. Heck, C. Ma, M. N. Sakib, D. Huang, H. Rong, *Journal of Lightwave Technology* **2021**, *39*, 5083.
- [35] S. M. Sze, *Semiconductor Devices: Physics and Technology*, John Wiley & Sons Singapore Pte. Limited, **2012**.
- [36] D. J. Moss, R. Morandotti, A. L. Gaeta, M. Lipson, *Nat Photonics* **2013**, *7*, 597.
- [37] W. Bogaerts, P. De Heyn, T. Van Vaerenbergh, K. De Vos, S. Kumar Selvaraja, T. Claes, P. Dumon, P. Bienstman, D. Van Thourhout, R. Baets, *Laser Photon Rev* **2012**, *6*, 47.
- [38] A. Slawska-Waniewska, A. Siemko, G. Serfözö, *J Magn Magn Mater* **1991**, *93*, 169.
- [39] K. P. Müller, J. Pelka, *Microelectron Eng* **1987**, *7*, 91.
- [40] F. Brücknerhoff-Plückelmann, J. Feldmann, H. Gehring, W. Zhou, C. D. Wright, H. Bhaskaran, W. Pernice, *Nanophotonics* **2022**, *11*, 4063.
- [41] A. Rizzo, A. Novick, V. Gopal, B. Y. Kim, X. Ji, S. Daudlin, Y. Okawachi, Q. Cheng, M. Lipson, A. L. Gaeta, K. Bergman, *Nat Photonics* **2023**, DOI 10.1038/s41566-023-01244-7.
- [42] A. Fawzi, M. Balog, A. Huang, T. Hubert, B. Romera-Paredes, M. Berekatain, A. Novikov, F. J. R. Ruiz, J. Schrittwieser, G. Swirszcz, D. Silver, D. Hassabis, P. Kohli, *Nature* **2022**, *610*, 47.
- [43] N. P. Jouppi, C. Young, N. Patil, D. Patterson, G. Agrawal, R. Bajwa, S. Bates, S. Bhatia, N. Boden, A. Borchers, R. Boyle, P. Cantin, C. Chao, C. Clark, J. Coriell, M. Daley, M. Dau, J. Dean, B. Gelb, T. V. Ghaemmaghami, R. Gottipati, W. Gulland, R. Hagmann, C. R. Ho, D. Hogberg, J. Hu, R. Hundt, D. Hurt, J. Ibarz, A. Jaffey, A.

- Jaworski, A. Kaplan, H. Khaitan, D. Killebrew, A. Koch, N. Kumar, S. Lacy, J. Laudon, J. Law, D. Le, C. Leary, Z. Liu, K. Lucke, A. Lundin, G. MacKean, A. Maggiore, M. Mahony, K. Miller, R. Nagarajan, R. Narayanaswami, R. Ni, K. Nix, T. Norrie, M. Omernick, N. Penukonda, A. Phelps, J. Ross, M. Ross, A. Salek, E. Samadiani, C. Severn, G. Sizikov, M. Snelham, J. Souter, D. Steinberg, A. Swing, M. Tan, G. Thorson, B. Tian, H. Toma, E. Tuttle, V. Vasudevan, R. Walter, W. Wang, E. Wilcox, D. H. Yoon, in *Proceedings of the 44th Annual International Symposium on Computer Architecture*, Association For Computing Machinery, New York, NY, USA, **2017**, pp. 1–12.
- [44] J. Li, S. Ren, Y. Li, L. Yang, Y. Yu, R. Ni, H. Zhou, H. Bao, Y. He, J. Chen, H. Jia, X. Miao, *Sci Adv* **2023**, *9*, eadf7474.
- [45] S. Bandyopadhyay, A. Sludds, S. Krastanov, R. Hamerly, N. Harris, D. Bunandar, M. Streshinsky, M. Hochberg, D. Englund, (*Preprint*) *arXiv*, 2208.01623, v1, submitted: August **2022**.
- [46] C. Huang, S. Fujisawa, T. F. de Lima, A. N. Tait, E. C. Blow, Y. Tian, S. Bilodeau, A. Jha, F. Yaman, H.-T. Peng, H. G. Batshon, B. J. Shastri, Y. Inada, T. Wang, P. R. Prucnal, *Nat Electron* **2021**, *4*, 837.
- [47] F. Ashtiani, A. J. Geers, F. Aflatouni, *Nature* **2022**, *606*, 501.
- [48] J. Wang, S. P. Rodrigues, E. M. Dede, S. Fan, *Opt Express* **2023**, *31*, 18871.
- [49] H. Gehring, M. Blaicher, W. Hartmann, W. H. P. Pernice, *OSA Contin* **2019**, *2*, 3091.
- [50] “FIB-SEM for FIB-centric nanofabrication,” can be found under <https://raith.com/product/velion/>, accessed: September **2023**.



- [51] B. Tatian, *Appl Opt* **1984**, 23, 4477.
- [52] K. Luke, Y. Okawachi, M. R. E. Lamont, A. L. Gaeta, M. Lipson, *Opt Lett* **2015**, 40, 4823.

### Table of Contents (ToC)



This work highlights a scalable and non-volatile technique for post-fabrication tuning of photonic circuits by automated silicon ion implantation to precisely align high quality resonant devices to targeted wavelengths. Spectral shifts ranging from less than a few picometres to several nanometres are obtained showing long-term stability without inducing additional loss. This approach is finally applied to photonic memory and computing systems, enabling wavelength multiplexed integrated architectures at large scales.